Cold-Season Precipitation Sensitivity to Microphysical Parameterizations: Hydrologic Evaluations Leveraging Snow Lidar Datasets

W. J. RUDISILL,[a] A. N. FLORES,[a] H. P. MARSHALL,[a] E. SIIRILA-WOODBURN,[b] D. R. FELDMAN,[b] A. M. RHOADES,[b] Z. XU,[b] AND A. MORALES[c,d]

[a] *Boise State University, Boise, Idaho*
[b] *Earth and Environmental Sciences Area, Lawrence Berkeley National Laboratory, Berkeley, California*
[c] *Cooperative Institute for Research in Environmental Sciences, University of Colorado Boulder, Boulder, Colorado*
[d] *NOAA Physical Sciences Laboratory, Boulder, Colorado*

(Manuscript received 5 December 2022, in final form 3 August 2023, accepted 19 October 2023)

ABSTRACT: Cloud microphysical processes are an important facet of atmospheric modeling, as they can control the initiation and rates of snowfall. Thus, parameterizations of these processes have important implications for modeling seasonal snow accumulation. We conduct experiments with the Weather Research and Forecasting (WRF V4.3.3) Model using three different microphysics parameterizations, including a sophisticated new scheme (ISHMAEL). Simulations are conducted for two cold seasons (2018 and 2019) centered on the Colorado Rockies' ~750-km^2 East River watershed. Precipitation efficiencies are quantified using a drying-ratio mass budget approach and point evaluations are performed against three NRCS SNOTEL stations. Precipitation and meteorological outputs from each are used to force a land surface model (Noah-MP) so that peak snow accumulation can be compared against airborne snow lidar products. We find that microphysical parameterization choice alone has a modest impact on total precipitation on the order of ±3% watershed-wide, and as high as 15% for certain regions, similar to other studies comparing the same parameterizations. Precipitation biases evaluated against SNOTEL are 15% ± 13%. WRF Noah-MP configurations produced snow water equivalents with good correlations with airborne lidar products at a 1-km spatial resolution: Pearson's *r* values of 0.9, RMSEs between 8 and 17 cm, and percent biases of 3%–15%. Noah-MP with precipitation from the PRISM geostatistical precipitation product leads to a peak SWE underestimation of 32% in both years examined, and a weaker spatial correlation than the WRF configurations. We fall short of identifying a clearly superior microphysical parameterization but conclude that snow lidar is a valuable nontraditional indicator of model performance.

KEYWORDS: Orographic effects; Cloud microphysics; Lidars/Lidar observations; Model evaluation/performance; Regional models; Mountain meteorology

1. Introduction

Precipitation (rain and snowfall) in mountains is highly variable in space and time, undersampled by weather stations and radar, and challenging to model and measure (Lundquist et al. 2019). In midlatitude regions, mountain precipitation often falls as snow, gradually accumulating as snowpacks that act as natural reservoirs supporting ecosystems and human systems across the watersheds into which they drain and beyond (Sturm et al. 2017; Siirila-Woodburn et al. 2021). The streamflow from snowmelt depends not only on the antecedent snow volume, but also on the spatial location of snow accumulation throughout the watershed (Luce et al. 1998; Kiewiet et al. 2022). The variability of snow accumulation occurs at a range of process scales spanning individual hillslopes to synoptic scales (Clark et al. 2011). The value of seasonal snowpack in the western United States has been estimated in the trillions of dollars (Sturm et al. 2017), yet spatial estimates of the water stored each winter remain poor in most areas. Snowfall is frequently the most uncertain forcing variable in snow energy and mass balance models, and therefore remains a critical but uncertain input for predicting this large natural reservoir (Raleigh et al. 2015).

A significant component of snowfall, and therefore where snowpacks accumulate, is caused by orographic enhancement resulting from a variety of dynamical mechanisms including stable upslope ascent from mechanical uplift, release of potential instabilities, lee-side convergence, seeder–feeder processes, and convection triggered by differential heating associated with changes in slope and aspect (Roe 2005; Houze 2012; Stoelinga et al. 2013; Kirshbaum et al. 2018). Convection-permitting atmospheric models (Prein et al. 2015) have demonstrated skill in modeling precipitation accumulation in mountain environments where orographic enhancement processes are important (Minder et al. 2008; Ikeda et al. 2010; Rasmussen et al. 2011; Gutmann et al. 2012; He et al. 2019; Rudisill et al. 2021). For these reasons, and because of deficiencies in gridded precipitation products (Henn et al. 2018), studies investigating the mountainous hydrologic cycle and water resource management now frequently use output from numerical weather or climate models (Lundquist et al. 2019; Meyer et al. 2023).

Supplemental information related to this paper is available at the Journals Online website: https://doi.org/10.1175/JHM-D-22-0217.s1.

Corresponding author: William Rudisill, williamrudisill@u.boisestate.edu

DOI: 10.1175/JHM-D-22-0217.1

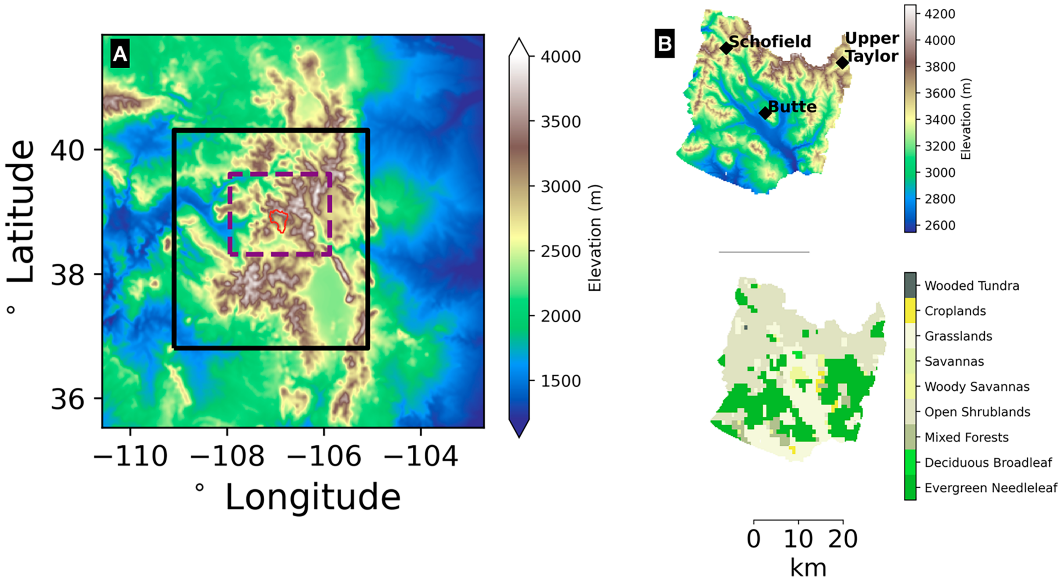

FIG. 1. (a) WRF model inner (black box) and outer (map extent) domains with elevation shown. The East River watershed (ERW) is outlined in red. The bounding box for drying-ratio calculations is also shown (purple dashed line). (b) The Noah-MP static geographic data used for snow modeling. Topography from the ASO lidar digital elevation model (DEM; top) and USGS 24 category vegetation classification type (bottom) are shown. Locations of NRCS SNOTEL locations (black diamonds) are also shown. The ASO domain extends slightly beyond the extent of the ERW.

However, the predicted precipitation fields from atmospheric models exhibit errors from a wide range of sources. For example, they are highly sensitive to the undertested assumptions in microphysical parameterizations (Liu et al. 2011; Minder and Kingsmill 2013; Comin et al. 2018; Rhoades et al. 2018; Rahimi et al. 2022). The problem is exacerbated in complex terrain where the location of falling precipitation upwind/downwind of an orographic barrier can have important hydrologic ramifications (Pavelsky et al. 2012). Unfortunately, the lack of comprehensive precipitation observations in complex terrain (Lundquist et al. 2019) creates an ill-posed process model development and diagnostic premise: modeled precipitation is highly sensitive to model structural and parameterization choices, but those choices are not easily evaluated with observations. This is because commonly used gridded precipitation datasets are highly uncertain in locations far away from observations and can differ substantially in mountain regions (Henn et al. 2018). Radar beams are frequently blocked in complex terrain limiting quantitative precipitation estimates (Maddox et al. 2002). Consequently, there is great need for better model evaluations in complex mountain terrain.

At the same time, airborne light detection and ranging (lidar) scanning is increasingly used to monitor watershed-scale montane snowpack and provides high spatial resolution (1–5-m scale) maps of snow depth (SD) and snow water equivalent (SWE) after making assumptions about density (Painter et al. 2016). This is a trove of useful information, as the water content of a seasonal snowpack tells us the lower bound of the antecedent precipitation for that location. For example, if the snowpack has one meter of water stored, and a model says that only 750 mm of precipitation accumulated in that region, then we know the model is underpredicting. Lidar SD is measured by first mapping the snow-free land surface from aircraft. Subsequent flights during the snow season record snow-top heights, which are differenced from the bare-ground elevation. The accuracy for snow-height measurements in flat terrain is considered ±8 cm for a 1-m swath (Deems et al. 2013; Painter et al. 2016) in several studies, although some have reported values as high as 20–30 cm for certain vegetation types (Tinkham et al. 2014). Lidar SD can then be combined with model-derived snow density estimates to produce spatial estimates of SWE. Densities can be modeled using energy balance modeling (Hedrick et al. 2018), and generally vary less (spatially) than SD (Sturm et al. 2010). Lidar flights represent only a single snapshot in time of the state of the snowpack, and snow density estimates are limited by small observational datasets of density in complex terrain. Still, when measured near the peak of the accumulation season, SWE can be a very close measure of the antecedent snowfall received at that point, minus water lost to ablation, and both positive and negative impacts of wind redistribution. Previous studies have leveraged the strong relationship between precipitation processes and snow accumulation patterns to scale precipitation forcings for use in hydrologic modeling (Vögeli et al. 2016; Pflug et al. 2021), to examine precipitation–elevation gradients (Kirchner et al. 2014), and to evaluate the skill of various precipitation datasets (Behrangi et al. 2018).

The goal of this study is several-fold. We seek to evaluate the sensitivities of simulated snowfall in the Weather Research and Forecasting (WRF) Model (Skamarock et al. 2019; Powers et al. 2017) to three different microphysical parameterizations (or "schemes") of varying complexity across the snow accumulation portions of two water years (WY; October–April of 2018 and 2019) covering the vicinity of Colorado's East River watershed (ERW) and surrounding regions (Fig. 1) We evaluate the Morrison et al. (2005), Thompson et al. (2008), and recently

developed Ice-Spheroids Habit Model with Aspect-ratio Evolution (ISHMAEL; Jensen et al. 2017) schemes. We seek to 1) determine if the WRF Model meteorology can produce snowpacks with similar spatial patterns and magnitudes to what is observed by Airborne Snow Observatory (ASO; Painter et al. 2016) snow lidar, 2) identify which microphysical scheme is better, if any, as compared to ASO and NRCS SNOTEL (Snow Telemetry) gauge data (Serreze et al. 1999), and 3) examine if the WRF Model does better than the PRISM (Parameter Regression on Independent Slopes; Daly et al. 2008) geostatistical precipitation product for matching the ASO snow product. The PRISM dataset is commonly used for precipitation model validation in the western United States (e.g., Liu et al. 2017) so it is a useful baseline to compare models against. Model point-scale biases of accumulated precipitation are evaluated against three NRCS SNOTEL sites within the domain (Fig. 1). To better understand precipitation sensitivity to microphysics parameterizations, we also use a "drying ratio" method to evaluate the efficiency of each model configuration for converting water vapor flux to precipitation, based on Eidhammer et al. (2018). We also examine cross-section views of atmospheric quantities across the ERW to better understand the differences between each WRF scheme. The ultimate motivation of this study is to improve modeling capabilities of mountain cryosphere processes, particularly in the water-resource essential Upper Colorado River basin where this study is located (Tillman et al. 2022).

2. Methods

a. Study area

We focus our analysis on the ERW near Crested Butte, Colorado. The ERW is a high-elevation (2500–3500 MSL), representative Rocky Mountain watershed and the location of numerous critical zone, snow, and hydrologic studies (Hubbard et al. 2018), as well as a recently deployed Department of Energy Atmospheric Radiation Measurement (ARM) field site (Feldman et al. 2021). The landcover types are predominantly open shrubland and evergreen needleleaf. The Airborne Snow Observatory (Painter et al. 2016) provides a lidar-based SD and SWE product for WY2018–2019 covering the ERW with one flight near peak snow accumulation for WY2018 and 2019. Consequently, this watershed is an ideal test bed for examining microphysical, precipitation, and snow processes, and model products will serve as guidance for hypothesis testing of ongoing field observation campaigns. The study region technically extends beyond the ERW boundaries into the Taylor and Castle Creek watersheds, as ASO data covers these regions as well, and doing so allows for comparisons against two additional NRCS SNOTEL monitoring sites.

b. Microphysical parameterizations

It has been repeatedly shown that the representation of microphysical processes in atmospheric models applied at regional to global scales can have a significant impact on modeled orographic precipitation magnitude and spatial variability (Khain et al. 2000; Gettelman et al. 2019; Liu et al. 2011; Rhoades et al. 2018). Fundamentally, the microphysical parameterization schemes in atmospheric models attempt to represent removal of atmospheric water from a given model grid cell based on kinematic and thermodynamic conditions (Khain et al. 2000; Morrison et al. 2020). Schemes in operational models typically use "bulk" approaches, where the hydrometeor mixing ratio (mass per mass of dry air), number concentrations (particles per unit volume), and other hydrometeor properties are predicted for a limited number of species (graupel, rain, snow, cloud water, etc.; Morrison et al. 2020). Figure 2 illustrates an idealized depiction of some of the most prominent cloud microphysical processes that control distributions of precipitation in mountain regions. Moist processes can also influence the dynamics through latent heat release (Jiang 2003) and interactions with radiation (Chen et al. 2018).

In this study we test the Thompson (Thompson et al. 2008; hereafter MP08), Morrison (Morrison et al. 2005; hereafter MP10) and ISHMAEL (Jensen et al. 2017; hereafter MP55) microphysical schemes (Table 1). Each scheme treats ice phase hydrometeors and growth processes in different ways. The MP10 and MP08 both use five separate hydrometeor categories—cloud liquid, cloud ice, snow, graupel, and rain—and predict mixing ratios for each. MP10 predicts the number concentration for ice, rain, snow and graupel, whereas MP08 only predicts the number concentration for rain. In MP10, all hydrometeors are assumed to be spherical, with mass–density relationships given by $m(D) = \pi/6\rho_s D^3$. MP08 is similar but describes snowflakes as approximately planar, with mass–diameter relationships given by $m(D) = 0.069D^2$. The most sophisticated scheme tested is MP55, which forecasts higher-order moments of hydrometeor species beyond mixing ratios and number concentrations at the expense of a higher computational cost. The MP55 scheme uses three ice categories in place of snow/graupel categories and models the evolution of snowflakes as oblate spheroids with two evolving axes a_i and c_i, such that the particle mass is given by $m(a, c) = \rho_i(4/3)\pi a_i^2 c_i$. Here, a_i is half the major axis for plate-like crystals and half the minor axis for column-like crystals, and c_i is half the minor axis for plate-like crystals and half the major axis for column-like crystals. Consequently, MP55 explicitly models both columnar and dendritic ice-habits (characterized by different a_i/c_i ratios), and the temperature dependent nucleation of each of these forms. It is important to note that the growth processes (e.g., collection, vapor deposition) depend on the particle aspect ratio. Although we highlight some of the differences across the three microphysics schemes, there are a variety of other differences between the schemes, and a full accounting is beyond the scope of the present study.

c. WRF Model configuration

This study tests precipitation from the Weather Research and Forecasting (WRF) Model version V4.3.3 and sensitivities to microphysical parameterizations therein (Skamarock et al. 2019; Powers et al. 2017). WRF solves the compressible, nonhydrostatic Euler equations using a third-order Runge–Kutta timestepping method. Both simulations use a two-way nested domain. Table 2 lists WRF subgrid-scale parameterization

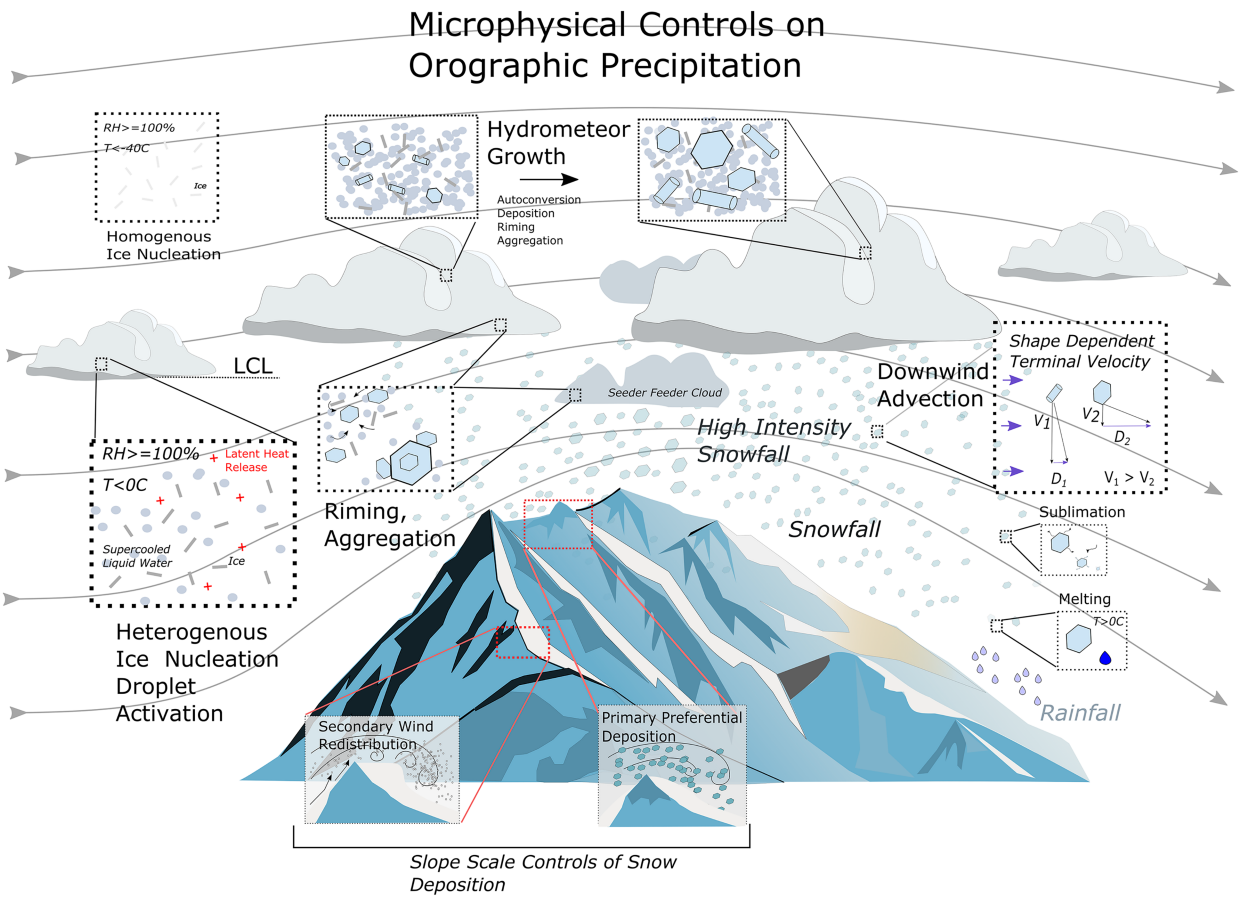

FIG. 2. Conceptual diagram illustrating key microphysical process controls on orographic precipitation as a parcel moves across a mountain barrier. The lifting condensation level (LCL), temperature (T), relative humidity (RH), hydrometeor velocity (V), and advection distance (D) are depicted. Secondary controls on slope scale snow deposition/redeposition are also shown. Gray contours show hypothetical wind streamlines.

schemes used in this study. Additional model configuration options including the entire WRF namelist are included in the online supplemental material. Lateral boundary and initial conditions for the WRF simulations are provided by the Climate Forecast System Reanalysis version 2 (CSFv2; Saha et al. 2014). CFSv2 has a 0.5° horizontal resolution (~55 km), and lateral boundary conditions are provided every 6 h. Two nested domains are used, a ~3-km outer (230 × 349 grid cells) and a ~1-km inner grid (349 × 391 grid cells). A two-week spinup period is used prior to the 1 October start date for each model run. The WRF meteorological outputs are then used to force a high-resolution (250 m dx/dy) offline configuration of the Noah-MP land surface model (Niu et al. 2011),

TABLE 1. Weather Research and Forecasting (WRF) Model V4.3.3 microphysics options examined in this study.

Scheme	Abbreviation	Reference
Thompson	MP08	Thompson et al. (2008)
Morrison	MP10	Morrison et al. (2005)
ISHMAEL	MP55	Jensen et al. (2017)

providing peak SWE and SD that are comparable to the spatial resolutions provided by the ASO lidar-derived snow product (50 m).

In this study, the WRF Model is run from 1 October 2017 to 30 April 2018 (part of WY2018) and from 1 October 2018 to 30 April 2019 (part of WY2019), respectively. These periods are chosen since they correspond with the typical snow-accumulation season for this watershed, and that the two ASO flight dates of interest are on 31 March 2018 and 7 April 2019, which are near the dates of peak SWE. In the paper we will refer to these time periods as WY2018 and WY2019 for convenience, even though they only represent the cold season part of the year, not the entire year. These years represent a fairly wet and a fairly dry cold season, so fortunately we can test the model for a range of snow conditions. Examining precipitation data from the NRCS Schofield SNOTEL site shows that WY2019 is the 8th wettest (172.8 mm above average) and WY2018 the 23rd wettest (−68.5 mm below average) out of 38 years of record. In addition, a fourth Noah-MP experiment is conducted using precipitation from the PRISM dataset (Daly et al. 2008). PRISM is a commonly used data product

TABLE 2. Weather Research and Forecasting (WRF) subgrid-scale physics parameterizations used in this study.

Physics parameterization	Option	Reference
Convection	None	—
Microphysics	Thompson (MP08)	Thompson et al. (2008)
	Morrison (MP10)	Morrison et al. (2005)
	Ismael (MP55)	Jensen et al. (2017)
LSM	Noah-MP	Niu et al. (2011)
Surface layer	Monin–Obukhov (option 2)	Monin and Obukhov (1954)
Planetary boundary layer	Mellor–Yamada–Janjic (Eta/NMM) PBL	Janić (2001)
Longwave radiation	Community Atmosphere Model (CAM)	Neale et al. (2010)
Shortwave radiation	Community Atmosphere Model (CAM)	Neale et al. (2010)

that is frequently used, either directly or indirectly, to generate spatial precipitation forcings for model applications (Lundquist et al. 2019), so this experiment serves as a useful benchmark test for the skill of WRF precipitation. PRISM is often used as a benchmark dataset for atmospheric model development studies, so it is a good test for the baseline of model performance.

d. Model performance metrics

The efficiency of each microphysical scheme is evaluated using the drying ratio (DR) method (Eidhammer et al. 2018), which is in essence the accumulated precipitation normalized by the flux of the integrated vapor transport. The components are given by

$$F_{u,x} = -\frac{1}{g}\int_{p_0}^{p_{\mathrm{Top}}}\int_x\int_t qU\,dP\,dx\,dt, \tag{1}$$

$$F_{v,y} = -\frac{1}{g}\int_{p_0}^{p_{\mathrm{Top}}}\int_y\int_t qV\,dP\,dy\,dt, \tag{2}$$

where p is atmospheric pressure, U and V are meridional and zonal winds, respectively, and q is the water vapor mixing ratio (kg kg^{-1}). The DR is then given by

$$\mathrm{DR} = \frac{P}{F}, \tag{3}$$

where $F = F_{v,y} + F_{u,x}$ and P is the mass of precipitation in kilograms. The DR calculation makes several assumptions, following Eidhammer et al. (2018). The assumptions are that nonvapor phases (clouds, ice, snow, etc.) are not included in the Q flux calculation [Eq. (2)], as the fraction of the total vapor is small. The contribution of local evaporation to local precipitation is also considered negligible. Year-to-year variation in precipitation accumulation could result from a fairly constant precipitation efficiency but moisture flux variability, precipitation efficiency variability alone, or a combination of both. The purpose of computing the drying ratio for the two study years is to help disentangle these factors. Eidhammer et al. (2018) used the DR to examine how the shapes of mountain ranges impact orographic precipitation for a single configuration of WRF. This study on the other hand examines one geographic region, but how the DR changes for different configurations of the WRF Model. The DR is computed on a 145 × 180 grid cell box surrounding the ERW (Fig. 1). The calculation is simplified as the direction of season average integrated vapor transport is uniformly from the southwest.

We apply several different metrics to evaluate model snowpack against ASO observations. Two primary quantities are assessed: the spatial locations of snow accumulation within the ERW, and the total watershed storage of snow at the evaluation time steps. The spatial locations of snow are important for modeling the temporal dynamics of snowmelt and runoff (Luce et al. 1998), while the total snow provides an estimate of the water contained in the snow reservoir.

To assess spatial pattern similarity, we use an objective function described in Demirel et al. (2018) and applied in a similar, recent snow modeling study (Wrzesien et al. 2022). This spatial efficiency (SPAEF) metric for two datasets x and y of length n is given by

$$\mathrm{SPAEF} = 1 - \sqrt{(1-\gamma)^2 + (1-\beta)^2 + (1-r)^2}, \tag{4}$$

where γ is the histogram intersection (Swain and Ballard 1991), given by

$$\gamma = \frac{\sum_{i=1}^{n}\min(K_i, J_i)}{\sum_{i=1}^{n} K_i}, \tag{5}$$

where K and J are the respective histograms for datasets x and y. The histogram bin size is set to 100. The β term in Eq. (4) is given by

$$\beta = \frac{\sigma_x}{\mu_x}\Big/\frac{\sigma_y}{\mu_y}, \tag{6}$$

where σ and μ are standard deviations and means of x and y, and r is the Pearson correlation coefficient (Pearson's r) and is given by

$$r = \frac{\sum_{i=0}^{n}(x_i - \bar{x})(y_i - \bar{y})}{\sqrt{\sum_{i=0}^{n}(x_i - \bar{x})^2 \sum_{i=0}^{n}(y_i - \bar{y})^2}}. \tag{7}$$

The histogram intersection is performed after normalizing the data (subtracting the mean and dividing by the standard deviation). Consequently, the SPAEF is designed to be a measure of spatial similarity between two datasets x and y that is insensitive to biases in those datasets (Demirel et al. 2018). A perfect value of SPAEF (equivalent x and y) is 1.

In addition to the SPAEF and the Pearson's r, we evaluate the percent bias (bias_p), given by

$$\text{bias}_p = \frac{\left(\sum_{i=1}^{n} x_i - \sum_{i=1}^{n} y_i\right)}{\sum_{i=1}^{n} y_i} \times 100. \tag{8}$$

The percent bias is insensitive to the spatial agreement of each dataset and is determined to measure watershed average snow quantity (depth or SWE) between the two datasets. Finally, we compute the root-mean-square error (RMSE), given by

$$\text{RMSE} = \sqrt{\frac{1}{n}\sum_{i=0}^{n}(x_i - y_i)^2}. \tag{9}$$

e. *Snowpack modeling, ASO data processing, and SNOTEL data comparison*

Snowpack spatial variability, at the peak of the accumulation season, is shaped by a combination of 1) precipitation variability, 2) slope scale preferential deposition, 3) secondary redistribution (e.g., blowing snow), and 4) melt/sublimation (or loss) processes (Mott et al. 2018; illustrated in Fig. 2). Avalanches also redistribute snow on steep slopes typically greater than 30°. To use ASO lidar snow data to evaluate precipitation variability, secondary redistribution and loss processes must be taken into account. The following sections describe how ASO data are processed for comparison purposes, and then how Noah-MP is configured to perform these tasks.

1) DATA PROCESSING

First, the ASO data in UTM spatial coordinates (downloaded from the NSIDC; https://nsidc.org/data/aso/data) data are clipped to the region of interest. The data are bilinearly resampled from 50 to 250 m using the "gdalwarp" algorithm (https://gdal.org/). The gdalwarp algorithm allows for several different resampling methods. Bilinear is chosen, following other studies that have similarly applied the same method to resample ASO snow products (Bair et al. 2016; Behrangi et al. 2018). The ASO data are then reprojected to a latitude–longitude coordinate system, again using the gdalwarp method, and converted to netcdf file format. At this stage, to enable grid-to-grid comparison, we use the xESMF python library (https://xesmf.readthedocs.io/en/latest/) and again select a bilinear interpolation method to align the ASO and Noah-MP model grids. We compared the total SD between converted ASO data and the raw data, and found that there was a very small difference overall. From there, we are able to compare the Noah-MP output grid cell to grid cell against the ASO data product. We chose an analysis scale of 1 km, as this matches the resolution of the parent WRF meteorology and wind-related features captured by ASO are likely smoothed out. To illustrate the effects, Fig. 3 shows the resampled SD data from 50 m to 1 km. Wind redistribution is clearly present on the windward/leeward sides of ridges at 50 m, but at 1 km these high-frequency features are removed. This step is performed using the xarray "coarsen" function.

Converting SD to snow water equivalent requires estimates of snow density. While ASO produces some density products using energy balance modeling, the snow densities distributed for 2018 and 2019 in the ERW were created using a linear regression between snow course observations of SD and density (ASO Inc. 2023, personal communication). Consequently we chose to use the distributed, spatially explicit snow densities produced by Noah-MP, averaged across the model runs produced by this study to produce SWE estimates from the ASO depth products.

2) THE NOAH-MP MODEL

We use the Noah-MP model to account for snow ablation prior to the date of the ASO flight and to model snow densities. Noah-MP can be used as a stand-alone land surface model, or can be coupled with atmospheric models such as WRF. Niu et al. (2011) provides a technical description of the model. We use the version of Noah-MP distributed with V5.1.1 of the WRF-Hydro (Gochis et al. 2018) modeling software, available online (https://github.com/NCAR/wrf_hydro_nwm_public/releases/tag/v5.1.1). Noah-MP solves the energy and mass budgets of a multilayer snowpack taking into account sublimation, snowmelt, snow liquid-water retention, and canopy interception among other processes. Noah-MP uses three snow layers. Noah-MP also uses a semitile approach, such that there are separate flux calculations for the vegetated and nonvegetated fraction of each grid cell. We use the same physics options that were implemented in the National Water Model configuration of Noah-MP (as described in the technical documentation) as the model was tested and vetted in a number of snow-dominated basins across the western United States. Parameterizations relevant to this work include using the CLASS snow-albedo scheme (Verseghy 1991), the Jordan precipitation phase option (Jordan 1991), Monin–Obukhov-type surface layer resistance for heat (option 1) (Brutsaert 1982), and option 3 for canopy radiation (Dickinson 1983; Sellers 1985). The full Noah-MP namelist configuration is included in the supplemental material.

In addition to ASO data, we compare time series of WRF precipitation against accumulated precipitation from three NRCS SNOTEL (Serreze et al. 1999) stations located in or near the ERW (Fig. 1). The Schofield, Butte, and Taylor stations are located to the north, in the center, and to the east of the ERW, respectively, and are each located approximately 20 km away from each other (Fig. 1).

The ERW is a high-elevation continental watershed with cold temperatures, so we hypothesize that both rain and melt prior to peak SWE are relatively minimal basinwide. This

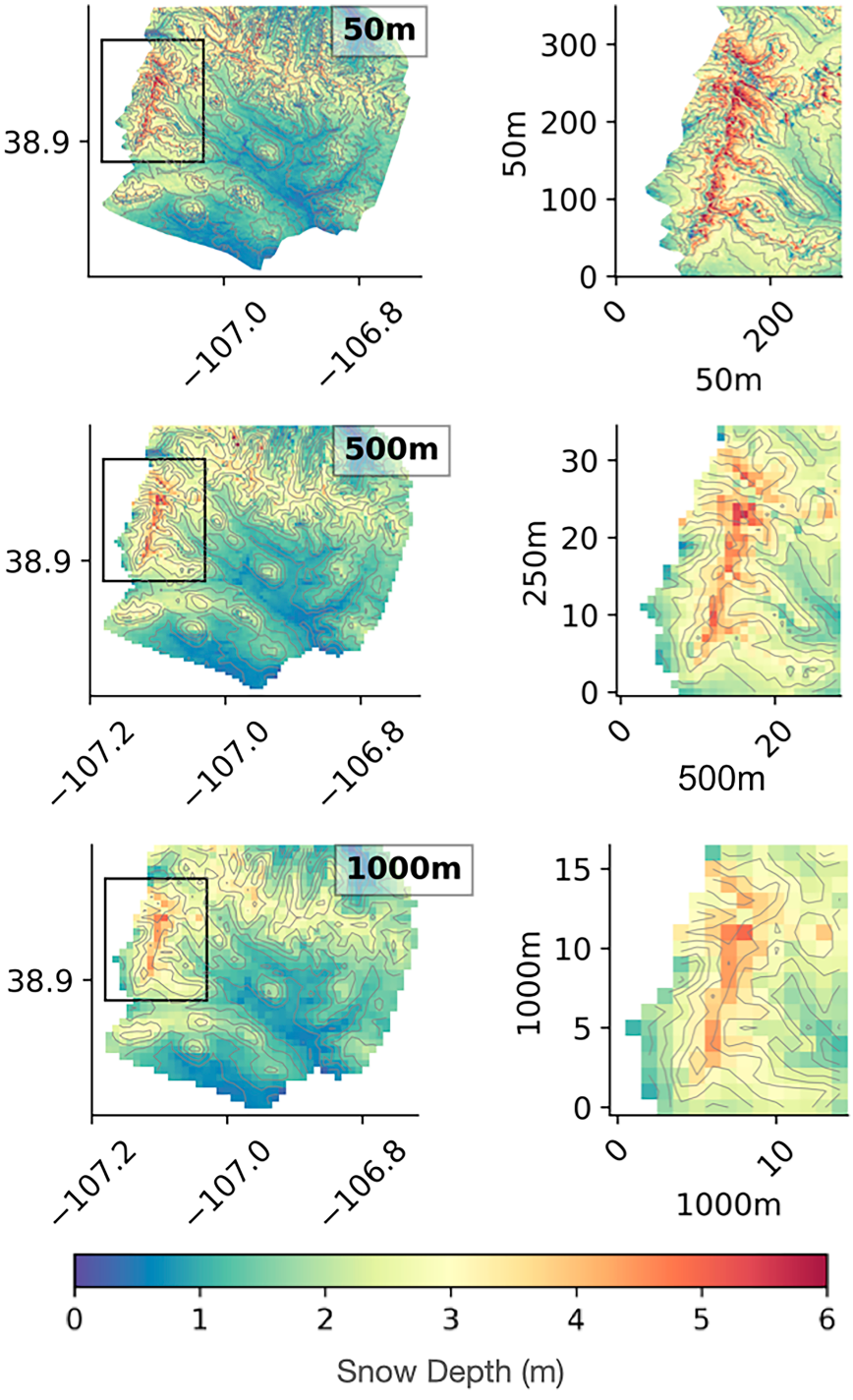

FIG. 3. Airborne Snow Observatory (ASO) lidar derived SD for 7 Apr 2019 at three different resolutions (50 m, 500 m, and 1 km) resampled using bilinear interpolation. The black box in the left panels corresponds to the latitudinal and longitudinal extent of the figures on the right.

hypothesis is confirmed by analyzing SNOTEL data in the watershed, as the 1 April SWE (recorded at the Butte SNOTEL snow pillow) is within ±2% of the accumulated precipitation (recorded at the collocated precipitation gauge) on 1 October for the two years examined (Fig. S1 in the online supplemental material) and average 2-m surface air temperatures are −4.5°C at the SNOTEL locations over the same time period. Nevertheless, Noah-MP and the nonprecipitation forcings are run and constructed for a 250-m regular latitude–longitude grid based on the high-resolution DEM distributed with ASO. This is done because,

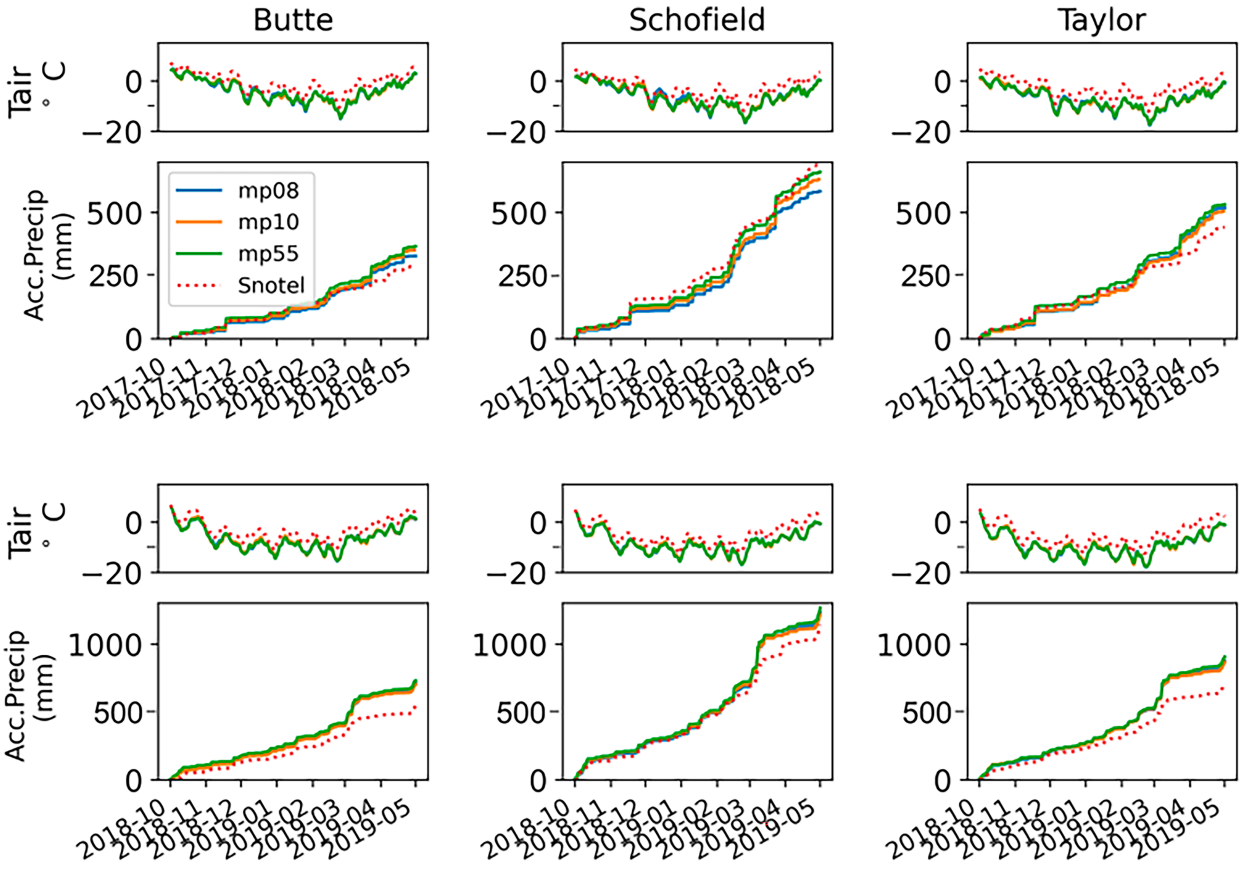

FIG. 4. Time series of WRF total accumulated precipitation (Acc. Precip; lower) and 2-m surface air temperature (Tair; upper) compared against three NRCS SNOTEL sites (Butte, Schofield, and Taylor) for WY2018 in the top rows and WY2019 in the bottom rows.

while antecedent melt might be small basinwide, forcing resolution and terrain-related effects are important for snow simulations and there may be south facing locations with significant midwinter ablation. Downscaling Noah-MP to 250 m is chosen, in part, based on results from Winstral et al. (2014), who examined the impact of various resolutions on snow simulation accuracy, and found that 250 m provided reasonable performance but was much degraded at coarser scales.

First, the hourly WRF output variables are bilinearly interpolated to the 250-m grid. Then, shortwave radiation, temperature, pressure, and specific humidity are adjusted to account for terrain differences between the digital elevation model distributed with WRF and the higher-resolution elevation model distributed by ASO. Temperature and pressure for each grid cell are adjusted via the constant dry adiabatic lapse rate and hydrostatic relationship to match the updated digital elevation model. Specific humidity is adjusted for elevation by assuming that the relative humidity (from the original WRF data) is conserved, and specific humidity is adjusted to match the corrected air temperature. The WRF downwelling shortwave radiation is converted to terrain-normal shortwave radiation using terrain geometry and solar angle relationships (Dingman 2015), using the slope and aspect from the high-resolution DEM. Terrain shadowing is not accounted for, but this impact is assumed to be minimal at 1-km resolution. Longwave radiation and winds are not adjusted, although corrections for terrain effects on shortwave and longwave radiation could improve the simulations (Arthur et al. 2018; Feldman et al. 2022) and could be pursued in future work. Some studies have further downscaled wind fields using empirical terrain relationships (Liston and Elder 2006) or physically based solvers (Reynolds et al. 2021). Since Noah-MP does not simulate wind redistribution, the benefits of more finely resolved wind fields are likely small (although wind velocities do control rates of latent/sensible heat). The code to perform the forcing corrections is available on GitHub (https://github.com/bsu-wrudisill/wrf_eriv_mphys_aso).

3. Results

a. *Precipitation accumulation evaluation*

The time series of WRF modeled precipitation and 2-m surface air temperature from each WRF microphysical scheme are compared against data from the three NRCS SNOTEL stations (Fig. 4). We do not show a comparison of PRISM against SNOTEL, since PRISM ingests SNOTEL information, so this would not constitute an independent validation. The spatial scale of orographic precipitation variability is

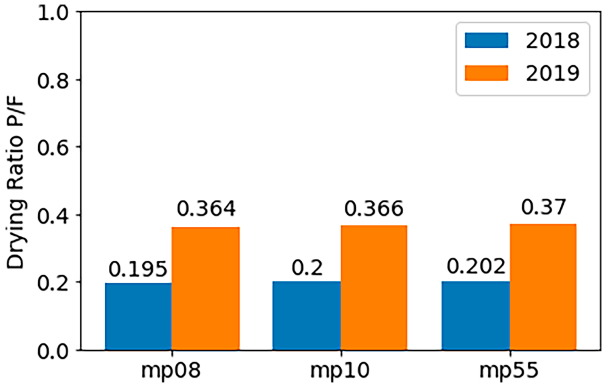

FIG. 5. Drying ratios (total precipitation normalized by incoming water vapor flux) computed for the greater ERW watershed region for 1 Oct–1 Apr for WY2018 and WY2019, for each WRF microphysics scheme.

apparent from looking at the SNOTEL data alone, as the Schofield station receives almost twice the precipitation of the Butte site, and each site receives almost double the precipitation in 2019 compared to the previous year (~1200 vs ~650 mm at Schofield, for example).

MP55 consistently produces the most precipitation (across all sites and both years), and MP08 generally has the least precipitation (all but the Taylor site in 2019; Fig. 4). The WRF simulated 2-m surface air temperatures are systematically cold biased by approximately 3°C across microphysical schemes. Evaluated against the NRCS SNOTEL stations, WRF has a bias of 15% ± 13% of accumulated precipitation at the end of the analysis period when averaged across each all of the years and WRF schemes. Across the three sites, the MP10 scheme performs the best for both WY2018 (9.5% bias) and the WY2019 (16% bias). These are just the biases from the three grid cells with SNOTEL observations. When the accumulated precipitation is averaged across the entire ERW (not just at SNOTEL locations) the WRF configurations differ by slightly more than 2% of accumulated precipitation, but different regions within the watershed differ by as much as 10%–15% (Fig. S2).

The differences in precipitation accumulations can be expressed as the efficiency of dynamical/microphysical processes for converting the incoming water vapor flux into precipitation. Figure 5 shows the DR averaged over 1 October–1 April for each scheme and each WY. MP55 consistently has the highest DR, with almost double the DR values from WY2018 to WY2019.

b. *Vertical atmospheric profiles*

The temporally averaged (1 October–1 April) cross section views of microphysical quantities, cross-sectional winds (*U* and *W* components), and vertical velocities show the different locations of ice-phase hydrometeor creation and fate, in addition to illuminating some of the precipitation relevant dynamics (Fig. 6). The ice phases are lumped together with snow and graupel for MP08 and MP10, the three ice species in MP55.

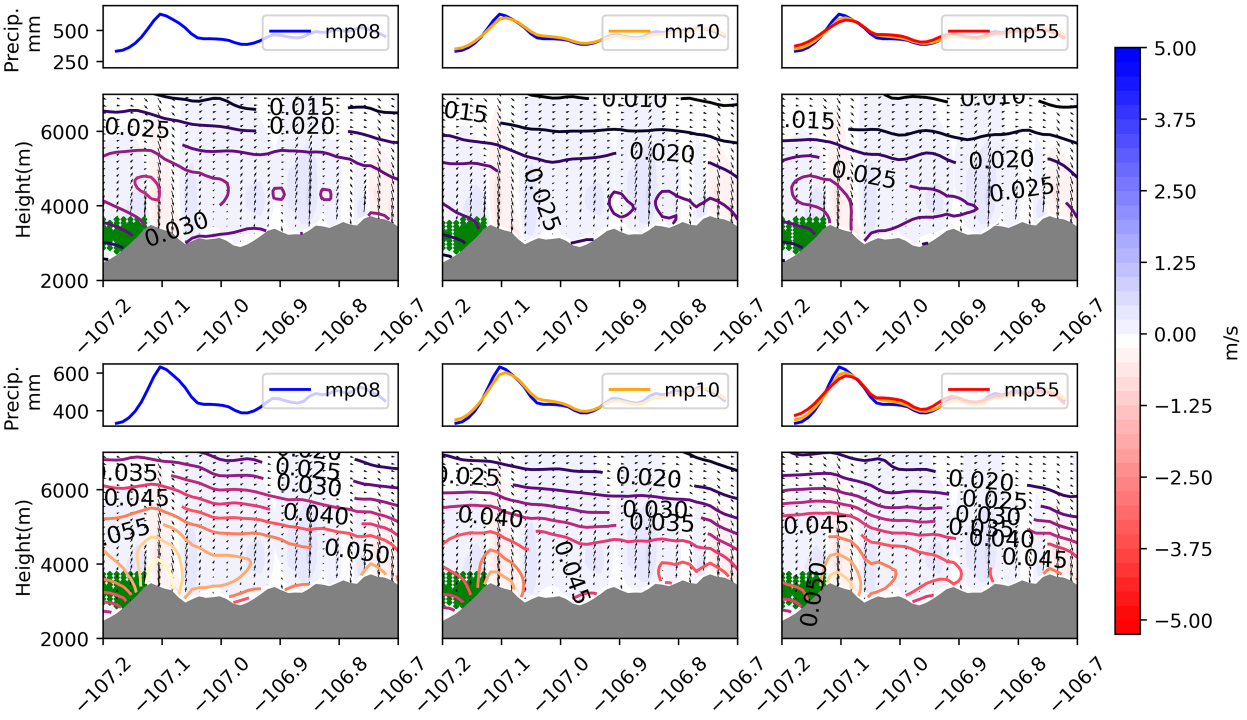

FIG. 6. Cross sections of average directions of vertical wind speed (red/blue shading; m s^{-1}), vertical and zonal flow (arrows; m s^{-1}), and ice-phase hydrometeor concentrations (contours; g kg^{-1} dry air). Green dots show the regions where the average meridional wind speed reverses and is greater than 1 m s^{-1}). Accumulated precipitation (precip) along the transect is shown (top plots). WY2018 is shown in the top two rows and WY2019 in the bottom two rows. The top of each plot shows cross sections of accumulated precipitation across the transect.

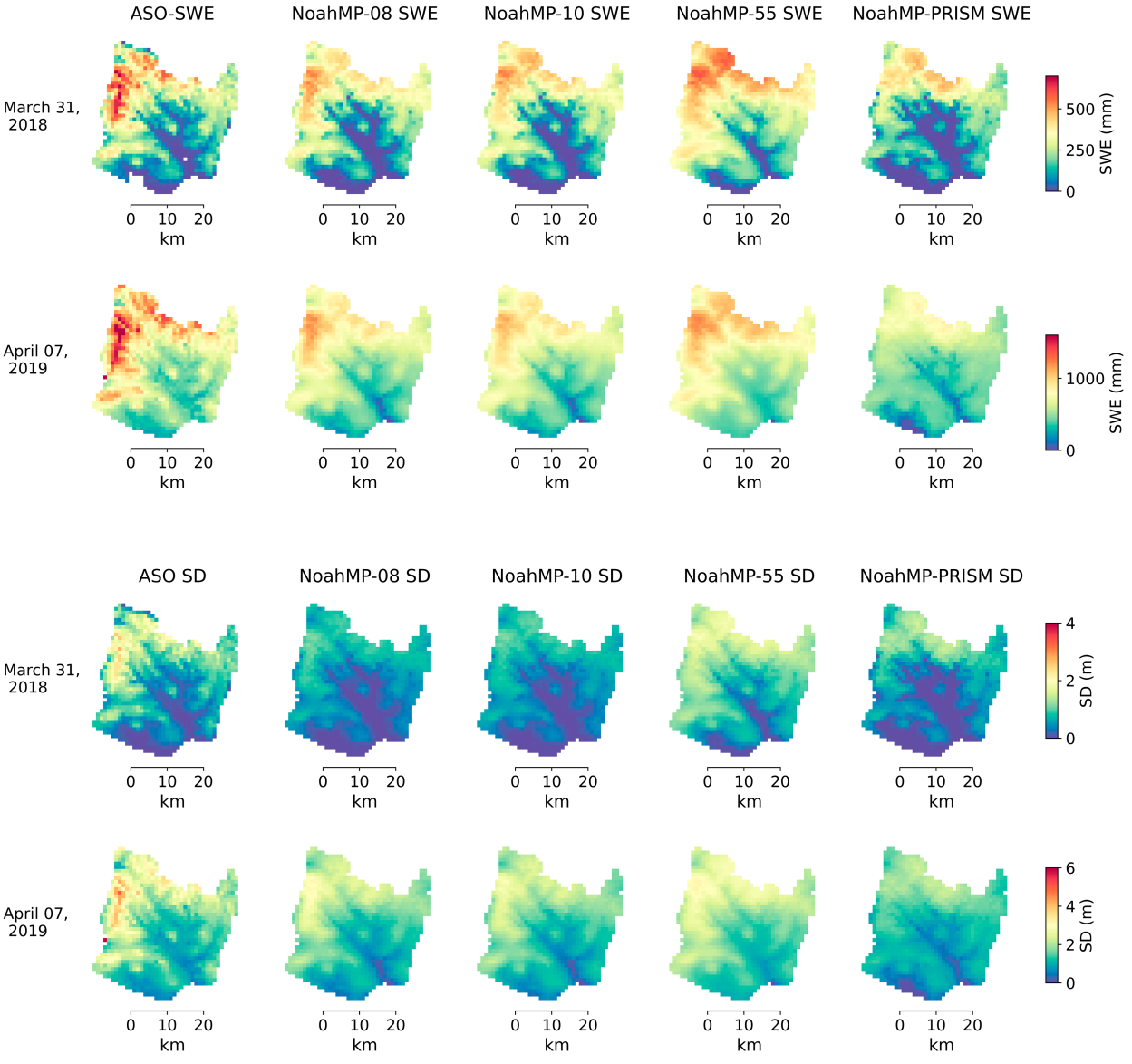

FIG. 7. Comparison of WY2018 and WY2019 SWE in the top two rows and SD in the bottom two rows from ASO and Noah-MP. The labels (08, 10, 55, and PRISM) refer to the precipitation forcing used for Noah-MP.

For all cases, the highest densities form a plume above the western watershed boundary, concentrated near the surface and decaying with height. MP55 has the highest densities across microphysical schemes, with a region of 3.0 g kg^{-1} during WY2018. There is a consistent negative vertical velocity component on the lee side of the western ridge (Fig. 6). Upstream of the ridge, there is a consistent low-level jet, characterized by a reversal in the zonal wind direction (northerly; green dots) relative to the zonal wind (southerly) on the lee side of the peak (not shown).

c. *Modeled SWE and SD–comparisons against ASO snow lidar*

Figure 7 shows the results of comparing SD and SWE between ASO lidar products and each Noah-MP model forced with the three WRF Model configurations (MP08; MP10; MP55) and a fourth test using the PRISM-based precipitation data. Air temperature, radiation, winds, and all other nonprecipitation meteorological forcings for the PRISM experiment come from the MP08 WRF run. To compare SWE from model results to the ASO lidar product, an estimate of snow density is still required. We chose to use the average density from the Noah-MP model rather than the ASO densities.

The fields from each model run are aggregated to a 1-km resolution from the native 250-m resolution for comparison of the final SWE values, and snow fields are plotted at the date of ASO acquisition (Fig. 7). The RMSE computed at several analysis resolutions were examined from 250 m to 8 km and we found the RMSE decreases asymptotically toward the

TABLE 3. Spatiotemporal and mass-balance error statistics for Noah-MP models compared against the ASO lidar derived basinwide SD and SWE estimates. Bold values denote the best performing scenario.

			Spatial		Mass balance	
Variable	Year	Model	r (unitless)	SPAEF (unitless)	RMSE (cm)	Bias (%)
Snow water equivalent (cm)	2018	Noah-MP-MP08	**0.914**	**0.878**	**8.453**	−15.498
		Noah-MP-MP10	0.905	0.870	8.603	−14.614
		Noah-MP-MP55	0.894	0.543	8.950	**12.043**
		Noah-MP-PRISM	0.821	0.805	13.133	−32.290
	2019	Noah-MP-MP08	**0.922**	**0.832**	15.947	−13.526
		Noah-MP-MP10	0.913	0.795	17.187	−14.713
		Noah-MP-MP55	0.908	0.688	**13.600**	**−2.576**
		Noah-MP-PRISM	0.785	0.706	30.605	−32.606
Snow depth (cm)	2018	Noah-MP-MP08	**0.913**	**0.902**	**26.798**	−15.039
		Noah-MP-MP10	0.903	0.888	27.254	**−13.823**
		Noah-MP-MP55	0.896	0.539	30.026	19.270
		Noah-MP-PRISM	0.840	0.783	43.084	−36.093
	2019	Noah-MP-MP08	**0.939**	**0.859**	39.281	−12.851
		Noah-MP-MP10	0.924	0.800	43.496	−14.669
		Noah-MP-MP55	0.917	0.604	**35.157**	**3.052**
		Noah-MP-PRISM	0.811	0.780	77.039	−32.765

mean difference between the respective datasets (not shown). The northwest region of the watershed collects the most snow compared to the rest of the watershed, a pattern that is consistent for both years. The snow accumulation in ASO does not simply follow topography, as the western ridge delineating the watershed boundary is higher elevation than the northwestern ridge, which collects more snow. ASO has a more variable pattern of snow accumulation and higher maxima than any of the WRF-forced Noah-MP cases for both WY. The PRISM case has a smaller proportion of snow in the northwestern region compared to ASO and the WRF cases.

Table 3 shows summary statistics of the SWE and SD comparisons. The ASO data are treated as the reference for computing the bias. MP08 has the highest Pearson's correlation coefficient for both SWE and SD for both years, and the PRISM case has the worst correlations. Still all WRF-forced cases have a good spatial correlation with the ASO SWE ($r = 0.9$). The PRISM precipitation forced case has the lowest skill of all of the categories examined. The PRISM case underestimates watershed total snow accumulation (~32%–36%) compared against the other WRF cases. The MP08 simulated SWE has the lowest RMSE (8.45 cm) but MP55 has the lowest percent bias for 2018 (12.0%). MP55 has the lowest RMSE and percent bias for 2019 (13.6 cm; −2.5%).

The trend between elevation and snow accumulation illustrates some additional important differences between ASO and WRF (Fig. 8). In each case, there is relatively little modeled melt except for the lower elevations (not shown). The average ASO SWE increase with elevation follows a linear pattern when a 200-grid-cell rolling-mean window is applied, which approximately flattens out above approximately 3500 m. The SD (not shown) shows the same leveling off, so this is a function of a decrease in depths, not just an artifact of modeled densities. The slope of the SWE versus elevation line is higher for WY2019 and parallels the 0.625 mm of SWE per meter of elevation, whereas 2018 more closely parallels the 0.50 mm m^{-1} line. The Noah-MP model SWE shows no such leveling out with elevation. The slopes of the Noah-MP curves are less steep than the ASO data and show the greatest spread during 2018. The variance of the ASO data increases with the magnitude (heteroskedasticity), which is not found in the WRF/Noah-MP modeled SWE.

4. Discussion

This is the first study, to our knowledge, that has used airborne lidar derived snow products to attempt to evaluate snowfall sensitivity to microphysical schemes in atmospheric models. To be clear, there are many other snow and atmospheric processes that must be understood to explain the elevation patterns of snow accumulation (Fig. 8) including high-elevation snow deposition, redistribution, and sublimation processes. The issue of scale mismatches between models (such as WRF with a 1-km grid spacing) and observations (such as meter-scale ASO lidar) presents a persistent challenge in snow hydrology and hydrology in general (Blöschl 1999). Atmospheric water delivery processes operate across a wide range of scales, from cloud-particle to synoptic weather (see Fig. 2), just as terrestrial processes influence snow variability. In this study, the decision was made to compute Noah-MP to ASO performance statistics at a 1-km resolution, rather than the 250-m resolution of the Noah-MP model. This choice aimed to address unresolved features, such as wind redistribution, which would likely contribute to model error (see Fig. 3), while still accounting for the impact of precipitation-induced variability. A natural question arises (see section 2): Why not run the model at 1-km resolution from the outset, without further downscaling of nonprecipitation forcings? Initial testing revealed that model performance degraded compared to the 250-m case, consistent with the findings of Winstral et al. (2014). Hence, the downscaling approach proved valuable for isolating the dominant error sources. Nevertheless, understanding

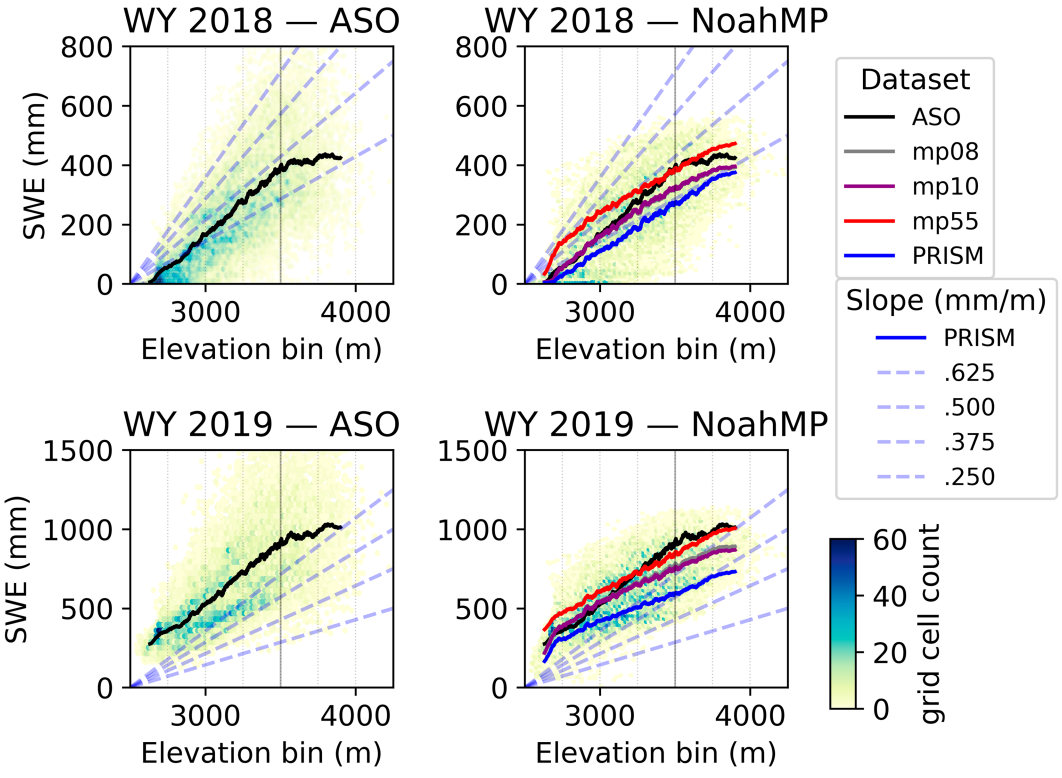

FIG. 8. SWE vs elevation relationships within the ERW. Density scatterplots of (left) ASO-derived SWE and (right) SWE from the Noah-MP simulations. The rolling-mean curves for the Noah-MP simulation and ASO product are shown. Lines with four different SWE vs elevation slopes (purple lines) are provided on each plot to better enable juxtaposition of datasets across different WY.

the relationship between process scales, data resolution, and model evaluation scales remains a crucial area of investigation. As argued by Blöschl (1999), optimal modeling element sizes are influenced by data availability and the required resolutions of model predictions. Following this philosophy, the model scale decisions in this study were carefully made.

Other studies have used snow lidar data to evaluate precipitation processes in various ways. Kirchner et al. (2014) evaluated both PRISM (Daly et al. 2008) precipitation and statistical SWE reconstructions against airborne lidar recorded near peak SWE accumulation in California. The tapering-off of the SD/SWE with elevation relationship found in the ERW (Fig. 8) was also observed in that study. Behrangi et al. (2018) used ASO data to evaluate several precipitation reconstructions in California's Tuolumne watershed. Our study found higher correlations between WRF/Noah-MP and ASO than any of the datasets examined in that study, but worse RMSE and biases (Behrangi et al. 2018; Table 3), which is also related to the scales of analysis (10 vs 1 km). The RMSEs between Noah-MP SWE and ASO SWE are similar to other reports comparing Noah-MP to ASO observations in Grand Mesa, Colorado (Wrzesien et al. 2022, their Fig. 12) at a similar resolution. Wrzesien et al. (2022) also used a genetic calibration algorithm to calibrate Noah-MP, a step that was not conducted here. Calibrating model parameters could possibly reduce model structural errors, further isolating the errors caused by model forcings; however, the similarity of errors with Wrzesien et al. (2022) suggests that Noah-MP is reasonably configured to model snow accumulation for this watershed and for the purposes of this study. Additionally, we should note that all Noah-MP models had higher SWE and SD values at the lowest elevations (less than 3000 m), which could be caused by a combination of underestimation in densification processes, too much precipitation in valley bottoms, and/or not enough melt or sublimation loss prior to the ASO lidar acquisition dates. Vegetation densities also change with elevation (Fig. 1), which may influence the aforementioned snow processes through snow–canopy interactions. Moreover, the heteroskedasticity of SWE/SD with elevation in the ASO products is another clear feature not well captured by Noah-MP. This could be due to avalanches or wind redistribution, which are not modeled by Noah-MP. Better capturing the ASO observed elevation–precipitation relationships in both atmospheric and snowpack models is a clear and testable objective for model improvement identified in this study.

More tightly coupling the land surface model and microphysical schemes may improve the study in a number of ways. The current version of Noah-MP does not accept solid/liquid precipitation phases as input, and instead uses a partitioning scheme from Jordan (1991). Near-surface air temperature–based methods do not always account for the range of microphysical processes, such as cooling from latent heat release

near the surface, that can lead to frozen phase precipitation accumulations at a wider range of temperatures (Jennings et al. 2018). This might be a major limitation in another watershed with lower elevations/warmer temperatures, but for each scheme tested a small percentage of the precipitation fell as rain, regardless of the partitioning method. Even after bias correcting the 2-m surface air temperatures uniformly across the domain for the −3°C bias compared against SNOTEL data (Fig. 4) only the modeled SWE values in the lowest elevations of the watershed were significantly impacted. Consequently, performance of the different microphysical schemes with respect to watersheds with larger rain–snow transition zones is untested and could be an area of future research.

Another interesting product of this research is the large modeled DR for WY2019. Eidhammer et al. (2018) reports lower DR more similar to that of WY2018, also for a region in Colorado, but for individual storm events as opposed to an entire cold season. Some of the differences are attributable to different WRF configurations and specific averaging regions used to compute the DR. This investigation shows the increase in DR largely responsible for the higher precipitation in 2019 compared to 2018, as opposed to an increase in water vapor flux, highlighting the role of precipitation generating dynamic mechanisms. DR values as high as 0.5 have been reported for the Andes (Smith and Evans 2007) so the quantities reported in 2019 (a maximum of 0.37) are not without precedent. The differences in DR between schemes could be a result of multiple factors. Differences in the treatment of heterogeneous ice-nucleation (Morrison et al. 2020) are one possible source of different computed DR. Additional work that examines specific microphysical tendencies could isolate these specifics in greater detail, such as the analysis performed in Bao et al. (2019).

a. *Snowpack density uncertainties and other potential improvements*

The largest uncertainty in estimating basinwide SWE from lidar derived snow-depth data comes from estimating snow density (Raleigh and Small 2017). In this study, we used snow densities simulated by Noah-MP to combine with ASO measured SD. In this way, the SWE and SD comparisons (Fig. 7) are not really independent. The density of new snow accumulation in the Noah-MP follows Hedstrom and Pomeroy (1998) and depends on the 2-m air temperature alone. Snowpack densification processes follow Anderson (1976) and Sun et al. (1999). ASO also distributes a density product that is based on energy balance and/or empirical depth modeling (ASO Inc. 2023, personal communication) but we chose to ignore it in this analysis. Incorporating snow density observations is one avenue for improving this work. Better coupling between the WRF microphysics scheme output and the snow model in Noah-MP could potentially improve simulated snow densities. The bulk snowpack density depends on density of new snow, snow metamorphosis, and compaction due to overburden (Colombo et al. 2019). Though untested in this study, modifying the Jensen (MP55) or Thompson (MP08) schemes and the Noah-MP code so that prognostic densities of snow and/or graupel are used by the land surface model, as opposed to recalculating snow densities in the land surface model, could potentially improve new snow density estimates. The Morrison scheme (MP10) does not treat snow or graupel density as a prognostic variable and the quantities are fixed at 100 and 500 kg m^{-3} respectively, so better coupling MP10 would be of less utility. Moreover, coupling advanced schemes such as MP55 that explicitly model hydrometeor shapes with snow process models may have additional utility for snow remote sensing applications, where grain geometries complicate the retrieval of snow properties from radar signals (Tsang et al. 2022).

Whether or not energetic forcings, such as shortwave and longwave radiation and sensible and latent heat fluxes, that contribute to snowmelt/densification are well represented is a significant source of uncertainty in this study. Three-dimensional longwave radiation effects from complex terrain are not considered by WRF and can be significant (Feldman et al. 2021). With that said, the observed cold bias in WRF has been observed in other climate models (Rhoades et al. 2018, 2022) and may potentially be related to longwave radiation processes, too-stable boundary layers over snow surfaces inhibiting heat exchanges (Slater et al. 2001), and/or other compensating biases (e.g., cloud cover). However, sensitivity tests showed that correcting for biases had relatively little effect on simulated peak SWE, particularly, for WY2019. Air temperatures at SNOTEL stations have also been shown to have quality control and calibration issues (Oyler et al. 2015) that may or may not be accounted for here, although comparisons with other meteorological station data near the watershed (not shown) suggests this alone does not explain the biases. Therefore, we caution to the hydrometeorological community that a more rigorous scrutiny of the temperature fields provided by WRF simulations in complex, high-elevation mountain terrain is needed. Comparing model outputs with ASO lidar datasets during the ablation season was not performed for this study, but could be another avenue to decompose simulated biases in temperature and radiation and identify systemic structural issues in the models, as the condition of the ablation season snowpack will be more sensitive to temperature and radiative forcings (in addition to other model parameterziations, like snow albedo) that cause snowmelt.

b. *Comparison with other microphysical parameterization sensitivity studies*

Ultimately, the sensitivity of precipitation accumulation to microphysics choice is similar to other studies that have compared the same options in WRF, but is much less than some that have examined a wider range of options in the WRF Model. Hughes et al. (2020) found that single-moment microphysics (WSM6) schemes were wetter than double-moment (Thompson/Morrison) when evaluated over a single WY in the Sierra Nevada, and that precipitation accumulation was more sensitive to microphysical parameterization choice than to lateral boundary conditions for convection-permitting WRF simulations in the Sierra Nevada. Xu et al. (2023) tested the sensitivity of WRF simulated meteorology to various subgrid parameterizations and boundary conditions for a subregion of

the ERW. They found that a suite of physics options using the WSM6 scheme led to 34% higher precipitation than simulations using the Thompson scheme, which is much higher than the sensitivity found comparing MP08, MP10, and MP55 in this study. Liu et al. (2011) examined a larger Colorado Rockies domain, and likewise found a modest ~2% difference between the MP08 and MP10 schemes for a 3-month period across a Colorado Rockies subdomain (Table 2 of their paper), with spatial pattern differences that are somewhat similar, but across a much larger area (Fig. 6 of their paper). The PLIN scheme (Chen and Sun 2002), however, also produced as much as 30% higher precipitation than the Thompson scheme. Interestingly, the PLIN scheme also showed a greater variance with elevation, which might better match reality in our study area (if snowpack is a good proxy; Fig. 8). Jensen et al. (2018) likewise compared MP08 and MP55 (in addition to several others) for a case study in the Olympic Peninsula. They determine that MP55 responds less strongly to topography than MP10 and two additional scenarios where hydrometeor growth in MP55 has been modified. Ultimately accumulated precipitation from MP55 differed from MP10 by less than 4% during their 18-h study period (Table 2 of their study), though it is unclear if that would change for longer evaluation period. Our simulation also produced very little graupel from either MP08 or MP10 (Fig. S3). Transitions from snow to graupel categories can introduce artificially abrupt transitions in particle properties (such as density and fall speed) and avoiding this is among the reasons that MP55 chooses to explicitly predict particle shapes rather than a graupel category (Jensen et al. 2018), so a simulation where atmospheric conditions are more favorable for graupel might show more spatial variability in precipitation. Ultimately, the precipitation sensitivity to microphysics choice was fairly modest averaged across the watershed, and in keeping with other studies that compared the same schemes. Testing other WRF options (such as PLIN or WSM6) might reveal a greater variance in snowfall accumulation and performance relative to ASO and SNOTEL.

Finally, while three schemes are tested in this study, each contains a range of parameters that each have an uncertainty space that has been underexplored, such as assumed concentrations of ice-nucleating particles. Idealized simulations show that perturbing individual parameters within individual microphysics schemes can have a similar impact to using an entirely different microphysics scheme (Morales et al. 2019). Future studies may consider producing an ensemble of simulations that sample across a plausible range of these parameter values, informed by new observational campaigns focused on mountain precipitation (Feldman et al. 2021).

5. Conclusions

High-altitude complex terrain is undergoing profound changes (Mountain Research Initiative EDW Working Group 2015) which are setting the stage for much-reduced snowpack in the coming years and decades (Siirila-Woodburn et al. 2021). The details of the snowfall that produces this snowpack are central to understanding the potential for changes in precipitation amount and phase. Nowhere is this more apparent than in the Upper Colorado River basin, which is dramatically stressed due to both long-term warming trends (Milly and Dunne 2020) and recent extreme drought (Williams et al. 2022). Since the East River watershed (ERW) represents a focused area of observations and research, collocated data and models of the ERW provide the opportunity to develop new tests of uncertain model processes.

This study used a high-resolution ASO lidar dataset of SD, collected near the peak of the snow accumulation season in the ERW, to evaluate precipitation for three different microphysical parameterizations (or schemes) implemented in the WRF Model for both a high precipitation (2019) and low precipitation (2018) cold season (October–April) prior to the dates of significant snowmelt. Model results show the magnitudes of precipitation between the years were more controlled by precipitation efficiencies (higher/lower DR) compared to increases/decreases in water vapor flux. All WRF configurations were able to capture the total precipitation evaluated at three NRCS SNOTEL sites, with an average bias of 15% ± 13% of accumulated precipitation at the end of the analysis period. The MP55 scheme had a slightly higher DR and better matched both SNOTEL and ASO observations for the high-snow volume year, but overpredicted precipitation and snowpack for the dry year (2018). Each microphysics scheme resulted in the development of snowpacks with a high spatial correlation with ASO lidar datasets at an ~1-km scale, but the Thompson (MP08) had the highest Pearson's correlation coefficient for both years examined. In terms of bias and correlation, all WRF Model configurations produced snowpacks that better matched ASO data, in particular in terms of bias, compared to the gauge-based statistical model estimates provided by the PRISM precipitation product with the exception of one measure of spatial similarity (SPAEF). Root-mean-square errors between the 1-km ASO lidar-based SWE and WRF Model products were on the order of 8–13 cm (WY2018) and 13–15 cm (WY2019). Underestimations of cold-season mountain precipitation from gridded products such as PRISM have been demonstrated in other circumstances (Lundquist et al. 2015; Lundquist et al. 2019).

This study found that ASO lidar snow datasets can potentially help evaluate microphysical scheme fidelity, but more importantly high-resolution regional climate models in poorly observed mountain regions in general. Model deficiencies that may or may not be related to microphysical process are also demonstrated, particularly with respect to snowpack/elevation patterns. While this study used only two ASO lidar flights, other studies with longer data coverage have shown repeatability of snow patterns to scale precipitation inputs into hydrologic models (Vögeli et al. 2016; Pflug et al. 2021). In the two ASO lidar flights used here, the locations of peak accumulation are consistently on the northwestern ridge of the ERW on the windward side and the location of strongest uplift. All models fail to create deep enough snowpacks in this region, highlighting a clear area of model improvement, although it remains to be seen if improved microphysical parameterizations, finer grid spacing, boundary conditions, or improvements to other model components are required to meet this challenge. Revisiting the three questions posed in

the introduction, we can conclude that 1) WRF and Noah-MP does match ASO snowpack with good fidelity, but certain features are not well captured (increasing snow depth variance with elevation; extreme accumulation on the northwest ridge of the watershed), 2) no single microphysics scheme emerges as clearly superior in terms of all of the criteria examined, and 3) WRF does perform better at matching the ASO snow products than the PRISM product.

The ability of any existing schemes to perform in out-of-sample conditions and additional constraints must be demonstrated as well. There is a potential to do this using field campaigns such as the Surface Atmosphere Integrated Field Laboratory (SAIL) for expanding upon the ASO lidar data collection presented in this study. Such data can and should be used to further constrain specific model microphysical process representations to establish if one or more schemes produce consistent results relative to observations across more hydroclimatological states than we tested here. We have demonstrated here that snowpack lidar products can be a useful diagnostic tool for microphysics parameterizations across two WY, but the question of whether snowpack surveys consistently constrain microphysics has not been demonstrated.

Acknowledgments. Rudisill was supported by the U.S. Department of Energy, Office of Science, Office of Workforce Development for Teachers and Scientists, Office of Science Graduate Student Research (SCGSR) program. The SCGSR program is administered by the Oak Ridge Institute for Science and Education (ORISE) for the DOE. ORISE is managed by ORAU under contract number DE-SC0014664. All opinions expressed in this paper are the authors' and do not necessarily reflect the policies and views of DOE, ORAU, or ORISE. Rudisill and Flores acknowledge additional funding from DOE BER grant DOE:DE-SC0019222. This research made use of Idaho National Laboratory computing resources, which are supported by the Office of Nuclear Energy of the U.S. Department of Energy and the Nuclear Science User Facilities under Contract DE-AC07-05ID14517. We also acknowledge high-performance computing support of the R2 compute cluster (https://doi.org/10.18122/B2S41H) provided by Boise State University's Research Computing Department. Rhoades was funded by the Director, Office of Science, Office of Biological and Environmental Research of the U.S. Department of Energy Regional and Global Climate Modeling Program (RGCM) "the Calibrated and Systematic Characterization, Attribution and Detection of Extremes (CASCADE)" Science Focus Area (Award DE-AC02-05CH11231) and the "An Integrated Evaluation of the Simulated Hydroclimate System of the Continental US" project (Award DE-SC0016605). Feldman's material was based upon work supported by the U.S. Department of Energy, Office of Science, Office of Biological and Environmental Research and the Atmospheric System Research under U.S. Department of Energy Contract DE-AC02-05CH11231. Morales was funded in part by the National Oceanic and Atmospheric Administration (NOAA) Cooperative Agreement with the Cooperative Center for Environmental Sciences (CIRES), NA17OAR4320101.

Data availability statement. Model outputs from the Noah-MP snow model and forcings are available on HydroShare (Rudisill 2023; WRF-Mphys-ERiv, HydroShare, http://www.hydroshare.org/resource/8b3a213f2a26474cb2d473cbb4b0ca19); see https://thredds.hydroshare.org/thredds/catalog/hydroshare/resources/8b3a213f2a26474cb2d473cbb4b0ca19/data/contents/catalog.html. Airborne Snow Observatory data are publicly available from the National Snow and Ice Data Center at https://nsidc.org/data/aso/data. PRISM precipitation data are available from https://prism.oregonstate.edu/.

REFERENCES

Anderson, E. A., 1976: A point of energy and mass balance model of a snow cover. NOAA Tech. Rep. NWS 19, 172 pp., https://repository.library.noaa.gov/view/noaa/6392/noaa_6392_DS1.pdf.

Arthur, R. S., K. A. Lundquist, J. D. Mirocha, and F. K. Chow, 2018: Topographic effects on radiation in the WRF model with the immersed boundary method: Implementation, validation, and application to complex terrain. *Mon. Wea. Rev.*, **146**, 3277–3292, https://doi.org/10.1175/MWR-D-18-0108.1.

Bair, E. H., K. Rittger, R. E. Davis, T. H. Painter, and J. Dozier, 2016: Validating reconstruction of snow water equivalent in California's Sierra Nevada using measurements from the NASA airborne snow observatory. *Water Resour. Res.*, **52**, 8437–8460, https://doi.org/10.1002/2016WR018704.

Bao, J.-W., S. A. Michelson, and E. D. Grell, 2019: Microphysical process comparison of three microphysics parameterization schemes in the WRF model for an idealized squall-line case study. *Mon. Wea. Rev.*, **147**, 3093–3120, https://doi.org/10.1175/MWR-D-18-0249.1.

Behrangi, A., K. J. Bormann, and T. H. Painter, 2018: Using the airborne snow observatory to assess remotely sensed snowfall products in the California Sierra Nevada. *Water Resour. Res.*, **54**, 7331–7346, https://doi.org/10.1029/2018WR023108.

Blöschl, G., 1999: Scaling issues in snow hydrology. *Hydrol. Processes*, **13**, 2149–2175, https://doi.org/10.1002/(SICI)1099-1085(199910)13:14/15<2149::AID-HYP847>3.0.CO;2-8.

Brutsaert, W., 1982: *Evaporation into the Atmosphere*. Kluwer Academic, 299 pp.

Chen, C.-A., and Coauthors, 2018: Falling snow radiative effects enhance the global warming response of the tropical Pacific atmosphere. *J. Geophys. Res. Atmos.*, **123**, 10 109–10 124, https://doi.org/10.1029/2018JD028655.

Chen, S.-H., and W.-Y. Sun, 2002: A one-dimensional time dependent cloud model. *J. Meteor. Soc. Japan*, **80**, 99–118, https://doi.org/10.2151/jmsj.80.99.

Clark, M. P., and Coauthors, 2011: Representing spatial variability of snow water equivalent in hydrologic and land-surface models: A review. *Water Resour. Res.*, **47**, W07539, https://doi.org/10.1029/2011WR010745.

Colombo, R., and Coauthors, 2019: Introducing thermal inertia for monitoring snowmelt processes with remote sensing. *Geophys. Res. Lett.*, **46**, 4308–4319, https://doi.org/10.1029/2019GL082193.

Comin, A. N., V. Schumacher, F. Justino, and A. Fernández, 2018: Impact of different microphysical parameterizations on extreme snowfall events in the Southern Andes. *Wea. Climate Extremes*, **21**, 65–75, https://doi.org/10.1016/j.wace.2018.07.001.

Daly, C., M. Halbleib, J. I. Smith, W. P. Gibson, M. K. Doggett, G. H. Taylor, J. Curtis, and P. P. Pasteris, 2008: Physiographically

sensitive mapping of climatological temperature and precipitation across the conterminous United States. *Int. J. Climatol.*, **28**, 2031–2064, https://doi.org/10.1002/joc.1688.

Deems, J. S., T. H. Painter, and D. C. Finnegan, 2013: Lidar measurement of snow depth: A review. *J. Glaciol.*, **59**, 467–479, https://doi.org/10.3189/2013JoG12J154.

Demirel, M. C., J. Mai, G. Mendiguren, J. Koch, L. Samaniego, and S. Stisen, 2018: Combining satellite data and appropriate objective functions for improved spatial pattern performance of a distributed hydrologic model. *Hydrol. Earth Syst. Sci.*, **22**, 1299–1315, https://doi.org/10.5194/hess-22-1299-2018.

Dickinson, R. E., 1983: Land surface processes and climate—Surface albedos and energy balance. *Advances in Geophysics*, Vol. 25, Elsevier, 305–353, https://doi.org/10.1016/S0065-2687(08)60176-4.

Dingman, S. L., 2015: *Physical Hydrology*. 3rd ed. Waveland Press, 643 pp.

Eidhammer, T., V. Grubišić, R. Rasmussen, and K. Ikdea, 2018: Winter precipitation efficiency of mountain ranges in the Colorado Rockies under climate change. *J. Geophys. Res. Atmos.*, **123**, 2573–2590, https://doi.org/10.1002/2017JD027995.

Feldman, D., and Coauthors, 2021: Surface Atmosphere Integrated Field Laboratory (SAIL) Science Plan. Tech. Rep. DOE/SC-ARM-21-004, 83 pp., https://www.arm.gov/publications/programdocs/doe-sc-arm-21-004.pdf.

——, M. Worden, N. Falco, P. J. Dennedy-Frank, J. Chen, B. Dafflon, and H. Wainwright, 2022: Three-dimensional surface downwelling longwave radiation clear-sky effects in the upper Colorado River basin. *Geophys. Res. Lett.*, **49**, e2021GL094605, https://doi.org/10.1029/2021GL094605.

Gettelman, A., H. Morrison, K. Thayer-Calder, and C. M. Zarzycki, 2019: The impact of rimed ice hydrometeors on global and regional climate. *J. Adv. Model. Earth Syst.*, **11**, 1543–1562, https://doi.org/10.1029/2018MS001488.

Gochis, D. J., and Coauthors, 2018: WRF-Hydro model source code version 5. UCAR/NCAR, https://doi.org/10.5065/D6J38RBJ.

Gutmann, E. D., R. M. Rasmussen, C. Liu, K. Ikeda, D. J. Gochis, M. P. Clark, J. Dudhia, and G. Thompson, 2012: A comparison of statistical and dynamical downscaling of winter precipitation over complex terrain. *J. Climate*, **25**, 262–281, https://doi.org/10.1175/2011JCLI4109.1.

He, C., F. Chen, M. Barlage, C. Liu, A. Newman, W. Tang, K. Ikeda, and R. Rasmussen, 2019: Can convection-permitting modeling provide decent precipitation for offline high-resolution snowpack simulations over mountains? *J. Geophys. Res. Atmos.*, **124**, 12 631–12 654, https://doi.org/10.1029/2019JD030823.

Hedrick, A. R., and Coauthors, 2018: Direct insertion of NASA airborne snow observatory-derived snow depth time series into the *iSnobal* energy balance snow model. *Water Resour. Res.*, **54**, 8045–8063, https://doi.org/10.1029/2018WR023190.

Hedstrom, N. R., and J. W. Pomeroy, 1998: Measurements and modelling of snow interception in the boreal forest. *Hydrol. Processes*, **12**, 1611–1625, https://doi.org/10.1002/(SICI)1099-1085(199808/09)12:10/11%3C1611::AID-HYP684%3E3.0.CO;2-4.

Henn, B., A. J. Newman, B. Livneh, C. Daly, and J. D. Lundquist, 2018: An assessment of differences in gridded precipitation datasets in complex terrain. *J. Hydrol.*, **556**, 1205–1219, https://doi.org/10.1016/j.jhydrol.2017.03.008.

Houze, R. A., Jr., 2012: Orographic effects on precipitating clouds. *Rev. Geophys.*, **50**, RG1001, https://doi.org/10.1029/2011RG000365.

Hubbard, S. S., and Coauthors, 2018: The East River, Colorado, watershed: A mountainous community testbed for improving predictive understanding of multiscale hydrological–biogeochemical dynamics. *Vadose Zone J.*, **17** (1), 1–25, https://doi.org/10.2136/vzj2018.03.0061.

Hughes, M., J. D. Lundquist, and B. Henn, 2020: Dynamical downscaling improves upon gridded precipitation products in the Sierra Nevada, California. *Climate Dyn.*, **55**, 111–129, https://doi.org/10.1007/s00382-017-3631-z.

Ikeda, K., and Coauthors, 2010: Simulation of seasonal snowfall over Colorado. *Atmos. Res.*, **97**, 462–477, https://doi.org/10.1016/j.atmosres.2010.04.010.

Janić, Z. I., 2001: Nonsingular implementation of the Mellor-Yamada level 2.5 scheme in the NCEP Meso model. NCEP Office Note 437, 61 pp.

Jennings, K. S., T. S. Winchell, B. Livneh, and N. P. Molotch, 2018: Spatial variation of the rain-snow temperature threshold across the Northern Hemisphere. *Nat. Commun.*, **9**, 1148, https://doi.org/10.1038/s41467-018-03629-7.

Jensen, A. A., J. Y. Harrington, H. Morrison, and J. A. Milbrandt, 2017: Predicting ice shape evolution in a bulk microphysics model. *J. Atmos. Sci.*, **74**, 2081–2104, https://doi.org/10.1175/JAS-D-16-0350.1.

——, ——, and ——, 2018: Impacts of ice particle shape and density evolution on the distribution of orographic precipitation. *J. Atmos. Sci.*, **75**, 3095–3114, https://doi.org/10.1175/JAS-D-17-0400.1.

Jiang, Q., 2003: Moist dynamics and orographic precipitation. *Tellus*, **55A**, 301–316, https://doi.org/10.3402/tellusa.v55i4.14577.

Jordan, R., 1991: A one-dimensional temperature model for a snow cover: Technical documentation for SNTHERM.89. Special Rep. 91-16, Cold Region Research and Engineers Laboratory, U.S. Army Corps of Engineers, Hanover, NH, 61 pp.

Khain, A., M. Ovtchinnikov, M. Pinsky, A. Pokrovsky, and H. Krugliak, 2000: Notes on the state-of-the-art numerical modeling of cloud microphysics. *Atmos. Res.*, **55**, 159–224, https://doi.org/10.1016/S0169-8095(00)00064-8.

Kiewiet, L., E. Trujillo, A. Hedrick, S. Havens, K. Hale, M. Seyfried, S. Kampf, and S. E. Godsey, 2022: Effects of spatial and temporal variability in surface water inputs on streamflow generation and cessation in the rain–snow transition zone. *Hydrol. Earth Syst. Sci.*, **26**, 2779–2796, https://doi.org/10.5194/hess-26-2779-2022.

Kirchner, P. B., R. C. Bales, N. P. Molotch, J. Flanagan, and Q. Guo, 2014: LiDAR measurement of seasonal snow accumulation along an elevation gradient in the southern Sierra Nevada, California. *Hydrol. Earth Syst. Sci.*, **18**, 4261–4275, https://doi.org/10.5194/hess-18-4261-2014.

Kirshbaum, D. J., B. Adler, N. Kalthoff, C. Barthlott, and S. Serafin, 2018: Moist orographic convection: Physical mechanisms and links to surface-exchange processes. *Atmosphere*, **9**, 80, https://doi.org/10.3390/atmos9030080.

Liston, G. E., and K. Elder, 2006: A meteorological distribution system for high-resolution terrestrial modeling (MicroMet). *J. Hydrometeor.*, **7**, 217–234, https://doi.org/10.1175/JHM486.1.

Liu, C., K. Ikeda, G. Thompson, R. Rasmussen, and J. Dudhia, 2011: High-Resolution simulations of wintertime precipitation in the Colorado headwaters region: Sensitivity to physics parameterizations. *Mon. Wea. Rev.*, **139**, 3533–3553, https://doi.org/10.1175/MWR-D-11-00009.1.

——, and Coauthors, 2017: Continental-scale convection-permitting modeling of the current and future climate of North

America. *Climate Dyn.*, **49**, 71–95, https://doi.org/10.1007/s00382-016-3327-9.

Luce, C. H., D. G. Tarboton, and K. R. Cooley, 1998: The influence of the spatial distribution of snow on basin-averaged snowmelt. *Hydrol. Processes*, **12**, 1671–1683, https://doi.org/10.1002/(SICI)1099-1085(199808/09)12:10/11<1671::AID-HYP688>3.0.CO;2-N.

Lundquist, J., M. Hughes, E. Gutmann, and S. Kapnick, 2019: Our skill in modeling mountain rain and snow is bypassing the skill of our observational networks. *Bull. Amer. Meteor. Soc.*, **100**, 2473–2490, https://doi.org/10.1175/BAMS-D-19-0001.1.

——, ——, B. Henn, E. Gutmann, B. Livneh, J. Dozier, and P. Neiman, 2015: High-elevation precipitation patterns: Using snow measurements to assess daily gridded datasets across the Sierra Nevada, California. *J. Hydrometeor.*, **16**, 1773–1792, https://doi.org/10.1175/JHM-D-15-0019.1.

Maddox, R. A., J. Zhang, J. J. Gourley, and K. W. Howard, 2002: Weather radar coverage over the contiguous United States. *Wea. Forecasting*, **17**, 927–934, https://doi.org/10.1175/1520-0434(2002)017<0927:WRCOTC>2.0.CO;2.

Meyer, J., J. Horel, P. Kormos, A. Hedrick, E. Trujillo, and S. M. Skiles, 2023: Operational water forecast ability of the HRRR-iSnobal combination: An evaluation to adapt into production environments. *Geosci. Model Dev.*, **16**, 233–250, https://doi.org/10.5194/gmd-16-233-2023.

Milly, P. C. D., and K. A. Dunne, 2020: Colorado River flow dwindles as warming-driven loss of reflective snow energizes evaporation. *Science*, **367**, 1252–1255, https://doi.org/10.1126/science.aay9187.

Minder, J. R., and D. E. Kingsmill, 2013: Mesoscale variations of the atmospheric snow line over the northern Sierra Nevada: Multiyear statistics, case study, and mechanisms. *J. Atmos. Sci.*, **70**, 916–938, https://doi.org/10.1175/JAS-D-12-0194.1.

——, D. R. Durran, G. H. Roe, and A. M. Anders, 2008: The climatology of small-scale orographic precipitation over the Olympic mountains: Patterns and processes. *Quart. J. Roy. Meteor. Soc.*, **134**, 817–839, https://doi.org/10.1002/qj.258.

Monin, A. S., and A. M. Obukhov, 1954: Osnovnye zakonomernosti turbulentnogo peremeshivanija v prizemnom sloe atmosfery (Basic laws of turbulent mixing in the atmosphere near the ground). *Tr. Geofiz. Inst., Akad. Nauk SSSR*, **24**, 163–187.

Morales, A., D. J. Posselt, H. Morrison, and F. He, 2019: Assessing the influence of microphysical and environmental parameter perturbations on orographic precipitation. *J. Atmos. Sci.*, **76**, 1373–1395, https://doi.org/10.1175/JAS-D-18-0301.1.

Morrison, H., J. A. Curry, and V. I. Khvorostyanov, 2005: A new double-moment microphysics parameterization for application in cloud and climate models. Part I: Description. *J. Atmos. Sci.*, **62**, 1665–1677, https://doi.org/10.1175/JAS3446.1.

——, and Coauthors, 2020: Confronting the challenge of modeling cloud and precipitation microphysics. *J. Adv. Model. Earth Syst.*, **12**, e2019MS001689, https://doi.org/10.1029/2019MS001689.

Mott, R., V. Vionnet, and T. Grünewald, 2018: The seasonal snow cover dynamics: Review on wind-driven coupling processes. *Front. Earth Sci.*, **6**, 197, https://doi.org/10.3389/feart.2018.00197.

Mountain Research Initiative EDW Working Group, 2015: Elevation-dependent warming in mountain regions of the world. *Nat. Climate Change*, **5**, 424–430, https://doi.org/10.1038/nclimate2563.

Neale, R. B., and Coauthors, 2010: Description of the NCAR Community Atmosphere Model (CAM5.0). NCAR Tech. Note NCAR/TN-486+STR, 283 pp., www.cesm.ucar.edu/models/cesm1.1/cam/docs/description/cam5_desc.pdf.

Niu, G.-Y., and Coauthors, 2011: The community Noah land surface model with multiparameterization options (Noah-MP): 1. Model description and evaluation with local-scale measurements. *J. Geophys. Res.*, **116**, D12109, https://doi.org/10.1029/2010JD015139.

Oyler, J. W., S. Z. Dobrowski, A. P. Ballantyne, A. E. Klene, and S. W. Running, 2015: Artificial amplification of warming trends across the mountains of the western United States. *Geophys. Res. Lett.*, **42**, 153–161, https://doi.org/10.1002/2014GL062803.

Painter, T. H., and Coauthors, 2016: The airborne snow observatory: Fusion of scanning lidar, imaging spectrometer, and physically-based modeling for mapping snow water equivalent and snow albedo. *Remote Sens. Environ.*, **184**, 139–152, https://doi.org/10.1016/j.rse.2016.06.018.

Pavelsky, T. M., S. Sobolowski, S. B. Kapnick, and J. B. Barnes, 2012: Changes in orographic precipitation patterns caused by a shift from snow to rain. *Geophys. Res. Lett.*, **39**, L18706, https://doi.org/10.1029/2012GL052741.

Pflug, J. M., M. Hughes, and J. D. Lundquist, 2021: Downscaling snow deposition using historic snow depth patterns: Diagnosing limitations from snowfall biases, winter snow losses, and interannual snow pattern repeatability. *Water Resour. Res.*, **57**, e2021WR029999, https://doi.org/10.1029/2021WR029999.

Powers, J. G., and Coauthors, 2017: The Weather Research and Forecasting Model: Overview, system efforts, and future directions. *Bull. Amer. Meteor. Soc.*, **98**, 1717–1737, https://doi.org/10.1175/BAMS-D-15-00308.1.

Prein, A. F., and Coauthors, 2015: A review on regional convection-permitting climate modeling: Demonstrations, prospects, and challenges. *Rev. Geophys.*, **53**, 323–361, https://doi.org/10.1002/2014RG000475.

Rahimi, S., W. Krantz, Y.-H. Lin, B. Bass, N. Goldenson, A. Hall, Z. J. Lebo, and J. Norris, 2022: Evaluation of a reanalysis-driven configuration of WRF4 over the western United States from 1980 to 2020. *J. Geophys. Res. Atmos.*, **127**, e2021JD035699, https://doi.org/10.1029/2021JD035699.

Raleigh, M. S., and E. E. Small, 2017: Snowpack density modeling is the primary source of uncertainty when mapping basin-wide SWE with lidar. *Geophys. Res. Lett.*, **44**, 3700–3709, https://doi.org/10.1002/2016GL071999.

——, J. D. Lundquist, and M. P. Clark, 2015: Exploring the impact of forcing error characteristics on physically based snow simulations within a global sensitivity analysis framework. *Hydrol. Earth Syst. Sci.*, **19**, 3153–3179, https://doi.org/10.5194/hess-19-3153-2015.

Rasmussen, R., and Coauthors, 2011: High-resolution coupled climate runoff simulations of seasonal snowfall over Colorado: A process study of current and warmer climate. *J. Climate*, **24**, 3015–3048, https://doi.org/10.1175/2010JCLI3985.1.

Reynolds, D. S., J. M. Pflug, and J. D. Lundquist, 2021: Evaluating wind fields for use in basin-scale distributed snow models. *Water Resour. Res.*, **57**, e2020WR028536, https://doi.org/10.1029/2020WR028536.

Rhoades, A. M., P. A. Ullrich, C. M. Zarzycki, H. Johansen, S. A. Margulis, H. Morrison, Z. Xu, and W. D. Collins, 2018: Sensitivity of mountain hydroclimate simulations in variable-resolution CESM to microphysics and horizontal resolution. *J. Adv. Model. Earth Syst.*, **10**, 1357–1380, https://doi.org/10.1029/2018MS001326.

——, and Coauthors, 2022: Asymmetric emergence of low-to-no snow in the midlatitudes of the American Cordillera. *Nat.*

Climate Change, **12**, 1151–1159, https://doi.org/10.1038/s41558-022-01518-y.

Roe, G. H., 2005: Orographic precipitation. *Annu. Rev. Earth Planet. Sci.*, **33**, 645–671, https://doi.org/10.1146/annurev.earth.33.092203.122541.

Rudisill, W., 2023: WRF-Mphys-ERiv. HydroShare, last accessed 18 December 2023, http://www.hydroshare.org/resource/8b3a213f2a26474cb2d473cbb4b0ca19.

——, A. Flores, and J. McNamara, 2021: The impact of initial snow conditions on the numerical weather simulation of a northern Rockies atmospheric river. *J. Hydrometeor.*, **22**, 155–167, https://doi.org/10.1175/JHM-D-20-0018.1.

Saha, S., and Coauthors, 2014: The NCEP Climate Forecast System version 2. *J. Climate*, **27**, 2185–2208, https://doi.org/10.1175/JCLI-D-12-00823.1.

Sellers, P. J., 1985: Canopy reflectance, photosynthesis and transpiration. *Int. J. Remote Sens.*, **6**, 1335–1372, https://doi.org/10.1080/01431168508948283.

Serreze, M. C., M. P. Clark, R. L. Armstrong, D. A. McGinnis, and R. S. Pulwarty, 1999: Characteristics of the western United States snowpack from Snowpack Telemetry (SNOTEL) data. *Water Resour. Res.*, **35**, 2145–2160, https://doi.org/10.1029/1999WR900090.

Siirila-Woodburn, E. R., and Coauthors, 2021: A low-to-no snow future and its impacts on water resources in the western United States. *Nat. Rev. Earth Environ.*, **2**, 800–819, https://doi.org/10.1038/s43017-021-00219-y.

Skamarock, W. C., and Coauthors, 2019: A description of the Advanced Research WRF Model version 4. NCAR Tech. Note NCAR/TN-556+STR, 145 pp., http://doi.org/10.5065/1dfh-6p97.

Slater, A. G., and Coauthors, 2001: The representation of snow in land surface schemes: Results from PILPS 2(d). *J. Hydrometeor.*, **2**, 7–25, https://doi.org/10.1175/1525-7541(2001)002<0007:TROSIL>2.0.CO;2.

Smith, R. B., and J. P. Evans, 2007: Orographic precipitation and water vapor fractionation over the Southern Andes. *J. Hydrometeor.*, **8**, 3–19, https://doi.org/10.1175/JHM555.1.

Stoelinga, M. T., R. E. Stewart, G. Thompson, and J. M. Thériault, 2013: Microphysical processes within winter orographic cloud and precipitation systems. *Mountain Weather Research and Forecasting: Recent Progress and Current Challenges*, F. K. Chow, S. F. J. De Wekker, and B. J. Snyder, Eds., Springer, 345–408.

Sturm, M., B. Taras, G. E. Liston, C. Derksen, T. Jonas, and J. Lea, 2010: Estimating snow water equivalent using snow depth data and climate classes. *J. Hydrometeor.*, **11**, 1380–1394, https://doi.org/10.1175/2010JHM1202.1.

——, M. A. Goldstein, and C. Parr, 2017: Water and life from snow: A trillion dollar science question. *Water Resour. Res.*, **53**, 3534–3544, https://doi.org/10.1002/2017WR020840.

Sun, S., J. Jin, and Y. Xue, 1999: A simple snow-atmosphere-soil transfer model. *J. Geophys. Res.*, **104**, 19 587–19 597, https://doi.org/10.1029/1999JD900305.

Swain, M. J., and D. H. Ballard, 1991: Color indexing. *Int. J. Comput. Vision*, **7**, 11–32, https://doi.org/10.1007/BF00130487.

Thompson, G., P. R. Field, R. M. Rasmussen, and W. D. Hall, 2008: Explicit forecasts of winter precipitation using an improved bulk microphysics scheme. Part II: Implementation of a new snow parameterization. *Mon. Wea. Rev.*, **136**, 5095–5115, https://doi.org/10.1175/2008MWR2387.1.

Tillman, F. D., N. K. Day, M. P. Miller, O. L. Miller, C. A. Rumsey, D. R. Wise, P. C. Longley, and M. C. McDonnell, 2022: A review of current capabilities and science gaps in water supply data, modeling, and trends for water availability assessments in the upper Colorado River basin. *Water*, **14**, 3813, https://doi.org/10.3390/w14233813.

Tinkham, W. T., A. M. S. Smith, H.-P. Marshall, T. E. Link, M. J. Falkowski, and A. H. Winstral, 2014: Quantifying spatial distribution of snow depth errors from lidar using random forest. *Remote Sens. Environ.*, **141**, 105–115, https://doi.org/10.1016/j.rse.2013.10.021.

Tsang, L., and Coauthors, 2022: Review article: Global monitoring of snow water equivalent using high-frequency radar remote sensing. *Cryosphere*, **16**, 3531–3573, https://doi.org/10.5194/tc-16-3531-2022.

Verseghy, D. L., 1991: CLASS—A Canadian land surface scheme for GCMS. I. Soil model. *Int. J. Climatol.*, **11**, 111–133, https://doi.org/10.1002/joc.3370110202.

Vögeli, C., M. Lehning, N. Wever, and M. Bavay, 2016: Scaling precipitation input to spatially distributed hydrological models by measured snow distribution. *Front Earth Sci.*, **4**, 108, https://doi.org/10.3389/feart.2016.00108.

Williams, A. P., B. I. Cook, and J. E. Smerdon, 2022: Rapid intensification of the emerging southwestern North American megadrought in 2020–2021. *Nat. Climate Change*, **12**, 232–234, https://doi.org/10.1038/s41558-022-01290-z.

Winstral, A., D. Marks, and R. Gurney, 2014: Assessing the sensitivities of a distributed snow model to forcing data resolution. *J. Hydrometeor.*, **15**, 1366–1383, https://doi.org/10.1175/JHM-D-13-0169.1.

Wrzesien, M. L., and Coauthors, 2022: Development of a "nature run" for Observing System Simulation Experiments (OSSEs) for snow mission development. *J. Hydrometeor.*, **23**, 351–375, https://doi.org/10.1175/JHM-D-21-0071.1.

Xu, Z., E. R. Siirila-Woodburn, A. M. Rhoades, and D. Feldman, 2023: Sensitivities of subgrid-scale physics schemes, meteorological forcing, and topographic radiation in atmosphere-through-bedrock integrated process models: A case study in the upper Colorado River basin. *Hydrol. Earth Syst. Sci.*, **27**, 1771–1789, https://doi.org/10.5194/hess-27-1771-2023